Electrospun Poly(3-hexylthiophene) Nanofibers with Highly Extended and Oriented Chains Through Secondary Electric Field for High-Performance Field-Effect Transistors

Jung-Yao Chen, Hung-Chin Wu, Yu-Cheng Chiu, Chih-Jung Lin, Shih-Huang Tung,* and Wen-Chang Chen*

An extra electric field is introduced below the spinneret in an electrospinning setup for producing poly(3-hexylthiophene) (P3HT) nanofibers. The liquid jet is greatly prolonged by the additional extensional force and thinner fibers can thus be obtained. The chain conformation and orientation in fibers are probed by differential scanning calorimetry and X-ray diffraction techniques. Under the influence of the secondary electric field, P3HT chains are extensively stretched and aligned along the fiber axis. The electrospun P3HT nanofibers are fabricated into field-effect transistors and the charge carrier mobilities of the nanofibers with and without secondary electric field are found to be 1.54×10^{-4} and 1.62×10^{-1} cm^2 V^{-1} s^{-1}, respectively. The dramatic enhancement of mobility by more than 1000 times is due to the effective charge transport through the delocalization of electrons along the highly extended and oriented P3HT backbones rather than the ordinary π–π stacking. In addition to P3HT, it is found that this simple method also works for poly(3-alkylthiophene).

1. Introduction

Conjugated polymer-based organic field-effect transistors (OFETs) have received considerable attention because of their low-cost, light weight, and flexibility.[1,2] Among this class of polymer, poly(3-alkylthiophene) (P3AT), especially poly(3-hexylthiophene) (P3HT), has been intensively investigated. P3HT is a solution-processable conjugated polymer with a high hole mobility up to 0.1–0.3 cm^2 V^{-1} s^{-1}.[3–5] The fundamental understanding of the charge transport in P3HT remains a challenge because of its complex molecular organization. Previous reports have shown that the intermolecular π–π stacking of the conjugated rings that allows holes to hop between polymer chains is the main transport mechanism in P3HT thin films where P3HT chains preferentially adopt an edge-on orientation with π–π stacking parallel to the substrate.[3,6] Thus, many efforts have been made to improve the π–π stacking of P3HT in order to obtain a high charge carrier mobility in OFETs.[7–11]

Nevertheless, recent studies provided another concept, that is, main-chain charge transport plays a more important role in the electrical properties of polymer semiconductors.[12–16] Theoretical analyses from quantum mechanics and molecular dynamics simulations have shown that the charge mobility along backbone is significantly higher than that along π–π stacking by 2–3 orders. Therefore, manipulating the orientation of polymer chains along channels should be a more efficient way to improve the charge carrier mobility in OFETs.[17] Various approaches, including friction-transfer,[13,16] film-straining,[14,15,18] flow-coating,[12] and solution shearing,[19] have been used to obtain an active layer with in-plane aligned polymer backbones. For the above alignment methods, however, the chain-directing is restricted by already-solidified films or strength insufficiency, and thus only a limited mobility enhancement, ≈1 order of magnitude, can be achieved.[13–15] To further improve the electrical performance, a stronger stress is required to effectively stretch and align polymer chains, and the highly extended, oriented states should be frozen before a large-scaled relaxation occurs.

Electrospinning has recently emerged as an alternative method of preparing nanometer-scaled polymer fibers for electronic device applications.[20–24] A similar process termed electrohydrodynamic printing technique has been developed to print large-area arrays of well-aligned nanofibers and to fabricate nano-channel transistors with high charge carrier mobility.[25,26] In this work, instead of aligning fibers, we take advantage of electrospinning technique to align polymer chains in fibers. A typical electrospinning process involves two primary stages: (1) a straight liquid jet ejected from the spinneret as the electrostatic force overcomes the surface tension, and (2) bending (whipping) instability of the jet caused by repulsive Coulomb force of the surface charges on the jet.[27–29] The magnitude of the strain rate during electrospinning is on

J.-Y. Chen, H.-C. Wu, Dr. Y.-C. Chiu,
C.-J. Lin, Prof. W.-C. Chen
Department of Chemical Engineering
National Taiwan University
Taipei 10617, Taiwan
E-mail: chenwc@ntu.edu.tw
Prof. S.-H. Tung, Prof. W.-C. Chen
Institute of Polymer Science and Engineering
National Taiwan University
Taipei 10617, Taiwan
E-mail: shtung@ntu.edu.tw

the order of 10^4 s^{-1}.[30] Such a strong elongation force tends to orient polymer chains along the stretching direction and induces anisotropic properties of fibers.[31–33] To further fortify the stretching effect, an external electric field, also called secondary electric field, provided by a charged ring in the pathway of liquid jet has been introduced into the typical electrospinning setup.[27,34] With the introduction of a secondary electric field, bending instability was shown to be dampened and the simulations demonstrated that the electric field can converge on the centerline above the collector to accelerate the solution jet and intensify the stretching force.[27]

In this study, we used the secondary electric field to strengthen the extensional force in P3HT-PMMA core-shell electrospinning process for stretching and aligning P3HT chains. The effects of the secondary electric field on the morphology and charge carrier mobility of P3HT nanofibers were investigated. Our experimental results indicate that by simply applying such an extra electric field, the P3HT chains are highly extended along the fiber axis, which in turn promotes the one-dimensional charge transport through P3HT main chains and leads to a significant improvement on the performance of P3HT nanofiber-based OFETs.

2. Results and Discussion

2.1. Electrospinning Process and Size of Electrospun Nanofibers

The electrospinning setup used in this study is shown in **Figure 1**a. An extra 8-cm diameter stainless steel ring connected to the power supply is placed 2 cm below the spinneret and creates the secondary electric field in the pathway of the liquid jet. The power supply provides the same voltage for the spinneret and the ring. Figure 1b,c is the CCD images of the jets from P3HT-PMMA coaxial electrospinning systems without and with the secondary electric field, respectively. The conductive ring is indicated by the dashed arrow in Figure 1c. In both cases, a straight liquid jet is ejected from the spinneret and then bended.

The difference is that the straight liquid jet is elongated from 3 to 5 cm with the presence of the secondary electric field, which is determined from the onset point of bending instability indicated by the solid arrows. In addition, the diameter of the area covered by fiber mat on the collector shrinks from 6.5 to 3.5 cm due to the dampening of the bending instability, as displayed in Figure 1d,e. The above observation demonstrates that the secondary electric field can prolong the liquid jet and strengthen the extensional force during electrospinning process.

The insertion of a secondary electric field not only prolongs liquid jets but also changes the diameter of electrospun fibers. **Figure 2** shows the FE-SEM images of the as-spun P3HT-PMMA core-shell fibers. The average diameters of the fibers without and with the secondary electric field are 2.11 and 1.39 μm, respectively. After removing PMMA by solvent etching, P3HT nanofibers without and with secondary electric field, denoted as PHTNF and PHTNF(II), respectively, are 414 and 144 nm in diameter, as shown in the insets of Figure 2a,b. The reduction in fiber diameter is due to a more elongated, thinner liquid jet caused by the secondary electric field.[27,35] In addition to the fiber size, this strong extensional force also greatly alters the conformation and orientation of P3HT chains in fibers and thus results in distinct thermal and electrical properties, as described below.

2.2. Thermal Behaviors of Nanofibers

Differential scanning calorimeter (DSC) was used to analyze the effect of electrospinning on the thermal properties of P3HT electrospun nanofibers. The representative DSC thermogram of pristine bulk P3HT (Figure S1a, Supporting Information) shows an endothermic peak at 230 °C, which is the melting temperature of the crystals formed by folded P3HT chains without special treatments.[36] **Figure 3** displays the DSC thermograms of P3HT electrospun fibers at a heating rate of 5 °C min^{-1}. For PHTNF sample (without the secondary electric field), an exothermic signal at 213 °C (T_c) followed by an endothermic one
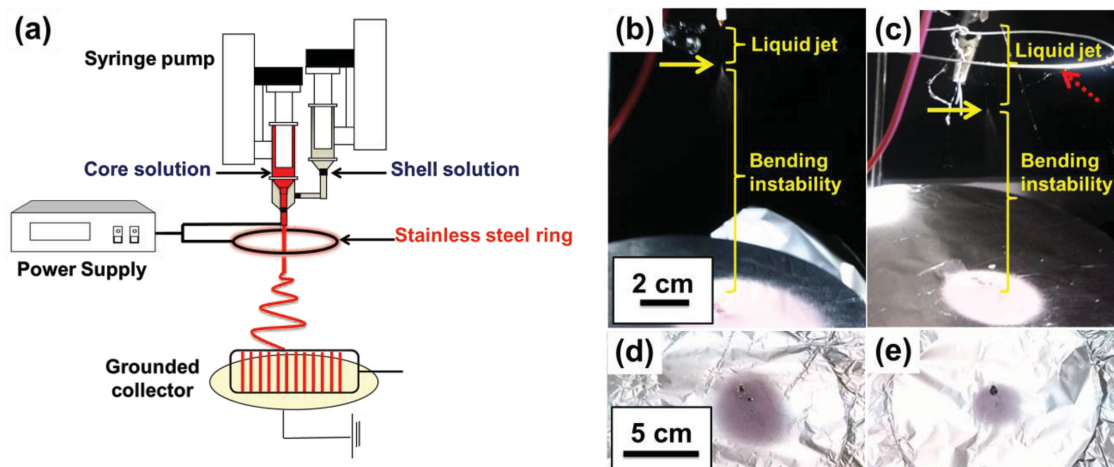

Figure 1. a) Schematic of the coaxial electrospinning setup with the secondary electric field, and the CCD images of the liquid jets and whipping ranges on the collectors for the setups without (b,d) and with (c,e) the secondary electric field, respectively. The red dashed arrow in (c) indicates the stainless steel ring.
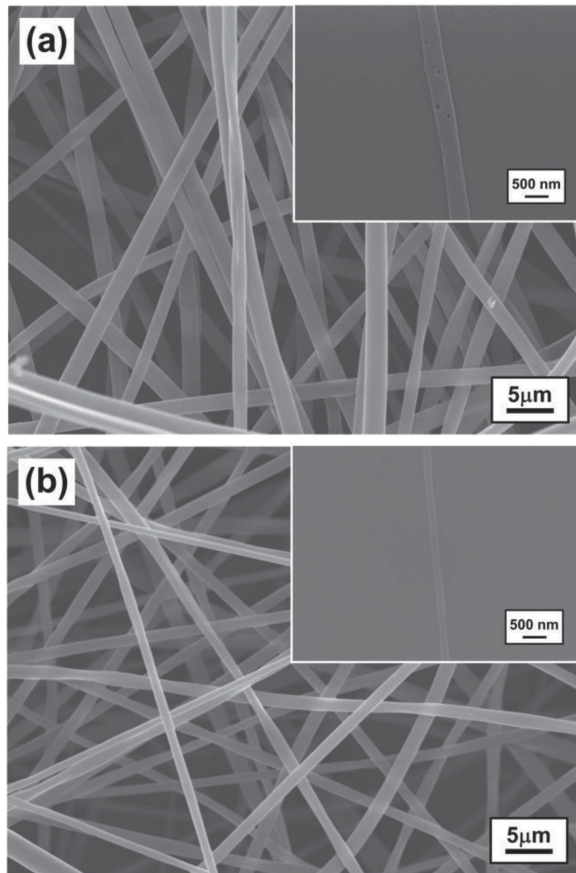
Figure 2. FE-SEM images of as-spun P3HT-PMMA core-shell fibers without a) and with b) the secondary electric field. The insects show the corresponding nanofibers, PHTNF, and PHTNF(II), respectively, after removing shell PMMA.

at 228 °C (T_{m1}) was observed, indicating that the fast drying process during electrospinning froze a portion of crystallizable P3HT chains in glassy states which then recrystallized and melted during subsequent heating. Another endothermic
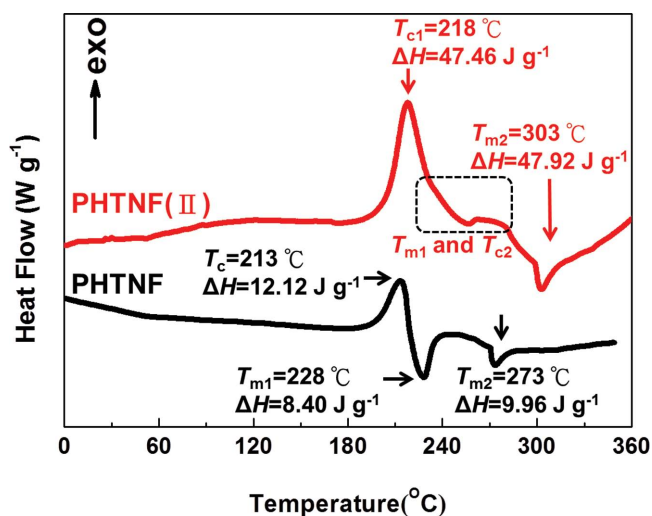

Figure 3. DSC thermograms of PHTNF and PHTNF(II).

peak (T_{m2}) was found at a higher temperature, ≈273 °C. It is well known that the melting point of polymer crystals increases with thickening of chain-folded crystal lamellae.[37] The higher melting point of PHTNF sample implies that the crystal lamellae are thicker than those of pristine P3HT. This is because the extensional force stretches chains during electrospinning and causes a longer length between two folding points. Note that the total endothermic heat is larger than the total exothermic heat in the heating profile, implying that some P3HT crystals are formed during electrospinning process.

For PHTNF(II) sample, a much more pronounced recrystallization exothermic signal can be seen at 218 °C (T_{c1}). Under the secondary electric field, the liquid jet becomes thinner and the evaporation of solvent is even faster due to the higher surface-to-volume ratio. In addition, the solvent in the inner part of the thinner jets can be completely dried in a shorter time. The crystallization of P3HT is therefore almost suppressed during electrospinning process and the kinetically frozen amorphous P3HT chains start to recrystallize after regaining mobility upon heating. Above T_{c1}, a rather complicated thermal behavior occurs, including an overlapping of the following transitions: the melting (T_{m1}) of the crystals formed around T_{c1}, another recrystallization at ≈270 °C (T_{c2}), and then another melting at a temperature as high as 303 °C (T_{m2}). Surprisingly, T_{m2} is even higher than the equilibrium melting point of P3HT ≈300 °C estimated in previous studies.[38,39] Note that the equilibrium melting point is defined as the melting point of crystals with infinite dimension, which implies that the crystals melted at 303 °C are formed by nearly fully extended P3HT chains. Furthermore, since the total heats of recrystallization and melting are approximately equal, the nearly perfect crystals are supposed to be formed upon heating, not during electrospinning process. We speculate that the strong extensional force produced by the secondary electric field fully stretches a significant fraction of P3HT chains, which are then frozen in glassy state due to the extremely rapid drying process. On following heating, the well-stretched and aligned chains form the nearly perfect crystals.

To verify the kinetically frozen P3HT chains in as-spun fibers, PHTNF(II) was isothermally crystallized at 218 °C for 12 h, named as PHTNF(II)-T, and the subsequent heating curve at a rate of 5 °C min^{-1} was recorded, as shown in Figure S1b (Supporting Information). Only one endothermic peak was observed at 230 °C and it is the same as the melting point of pristine P3HT, suggesting that under isothermal crystallization at 218 °C for a sufficient time, the stretched P3HT chains originally frozen in PHTNF(II) are completely relaxed and folded into crystals with thickness similar to those unaffected by external forces. The disappearance of endothermic peak at 303 °C for PHTNF(II)-T sample confirms that the nearly perfect crystals of PHTNF(II) revealed in Figure 3 are formed in the heating process, presumably above 270 °C (T_{c2}). When PHTNF(II) sample is heated at a rate of 5 °C min^{-1} (Figure 3), the less stretched chains recrystallize into folded lamellae around 218 °C (T_{c2}), but the time frame is too short for the fully extended chains to form crystals. The nearly perfect crystals can be formed above 270 °C in a short time scale because of the following two aspects: first, polymers tend to form thicker lamellae at a higher crystallization temperature (i.e., a smaller

supercooling), and second, the already aligned chains require only a short-range diffusion to pack closely and this can be easily achieved at a high temperature. We will show later that the highly extended P3HT chains in as-spun PHTNF(II) samples are crucial in enhancing the charge carrier mobility along the fibers.

2.3. Chain Packing and Orientation in Naonfibers

The molecular packing in P3HT nanofibers was probed by transmission-mode wide angle X-ray scattering (WAXS) and two-dimensional grazing incidence X-ray scattering (2D GIXS). From the transmission-mode WAXS profiles shown in **Figure 4**, the prominent (100) and relatively weak (200) and (300) diffraction peaks originating from the stacking of hexyl side chains, and the (010) diffraction from the π–π stacking between thiophenes are seen for both PHTNF and PHTNF(II). However, the broader (010) peak and stronger amorphous halos for PHTNF(II) sample implies that the strong stretching force and rapid drying process prevent P3HT chains from a long-range order packing, consistent with the DSC results that the crystallization is nearly suppressed under the secondary electric field.

2D GIXS techniques measured across and along the fibers were used to examine the orientation of P3HT packing in nanofibers as shown in **Figure 5**. For PHTNF, the intensities of the (100) and (010) diffractions are both stronger in q_z direction (out-of-plane) when the incident beam is perpendicular to the fiber axis (Figure 5a). The stronger (100) diffraction in q_z direction suggests that P3HT chains prevalently adopt an "edge-on" arrangement with respect to the fiber surface, similar to the preferential arrangement of P3HT in thin films with respect to the substrate.[40–42] The c-axis of P3HT crystal lamellae, i.e., P3HT backbone axis, is approximately along the fiber axis due to the stretching effect, which causes the (010) diffraction stronger in q_z direction. The structure of PHTNF is proposed in **Figure 6**a and this structure leads to the ring-like (100) and (010) diffraction patterns when the incident beam is parallel to the fiber axis as shown in Figure 5b. Note that in such a

structure, the direction of π–π stacking is approximately perpendicular to the fiber axis, and as shown by DSC data, P3HT chains are folded in crystal lamellae. In other words, neither π–π stacking route nor backbone route is effective for holes to move along the fibers in this case.

After applying the secondary electric filed, the (100) diffraction of PHTNF(II) becomes more ring-like with the incident beam perpendicular to the fiber axis (Figure 5c), i.e., the stacking of hexyl side chains become more randomly oriented in fibers. This can be attributed to the rapid drying process that inhibits P3HT chains from arranging in a regular "edge-on" manner which requires a sufficient time for hexyl side chains to move to fiber surface. The (010) diffraction of PHTNF(II) still dominates in the q_z direction, indicating that most P3HT main chains are along the fiber axis. The diffraction pattern with the incident beam parallel to fibers is shown in Figure 5d and as expected, more uniform (100) and (010) diffractions along azimuthal angle can be seen. Combining DSC and GIXS data, P3HT chains in PHTNF(II) are suggested to be highly extended and aligned along the fibers, as illustrated in Figure 6b, which provides a low-resistant pathway for charge carriers. After thermal treatment at 218 °C for 12 h, PHTNF(II)-T displays sharp, uniform (100) and (010) diffraction rings in both perpendicular and parallel measurements (Figure 5e,f), demonstrating the originally stretched P3HT chains are relaxed and form randomly oriented crystallites.

2.4. Electrical Properties of Naonofiber-Based OFETs

The electrical characteristics of P3HT nanofiber-based OFETs are shown in **Figure 7** and the parameters are summarized in **Table 1**. Figure 7a,b shows typical transfer characteristics of aligned PHTNF and PHTNF(II) devices. Compared to PHTNF, the drain current (I_{DS}) of PHTNF(II) devices as a function of gate voltage (V_{GS}) are more stable. Figure 7c presents the output properties of PHTNF(II) and the I_{DS} versus drain voltage (V_{DS}) curves show good field-effect characteristics with well-defined linear and saturation regimes. The average field-effect mobilities (μ_{ave}) of PHTNF and PHTNF(II) are 1.54×10^{-4} and 1.62×10^{-1} cm^2 V^{-1} s^{-1}, respectively. After applying the secondary electric field, the mobility of electrospun P3HT nanofibers is enhanced by more than 3 orders of magnitude. Recent reports have experimentally demonstrated that one-dimensional backbone delocalization is an efficient way to deliver charge carriers[13,15,16] and the simulation indicated that the theoretical value of the hole mobility along P3HT main chains is as high as 1 cm^2 V^{-1} s^{-1}.[17] We thus attribute the significant improvement of charge carrier mobility in PHTNF(II) to the highly extended P3HT chains along fibers under the strong extensional forces produced by the secondary electric field, while the low mobility of PHTNF is due to the lack of effective transport routes, as evidenced by the DSC and GIXS analyses. The transfer characteristics of PHTNF(II)-T device is compared with that of PHTNF(II) in Figure 7d. After annealing at 218 °C for 12 h, although the crystallinity is significantly increased, the randomly oriented crystallites cause the charge carrier mobility to sharply decrease to 2.26×10^{-5} cm^2 V^{-1} s^{-1}, even lower than that of PHTNF device. The results manifest the critical role of chain
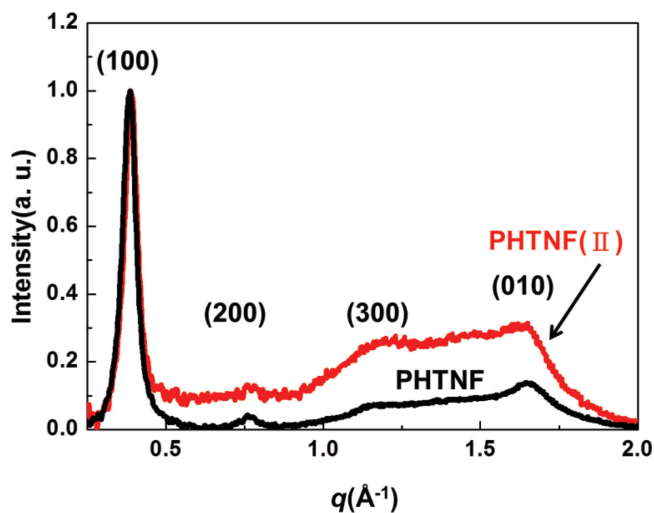

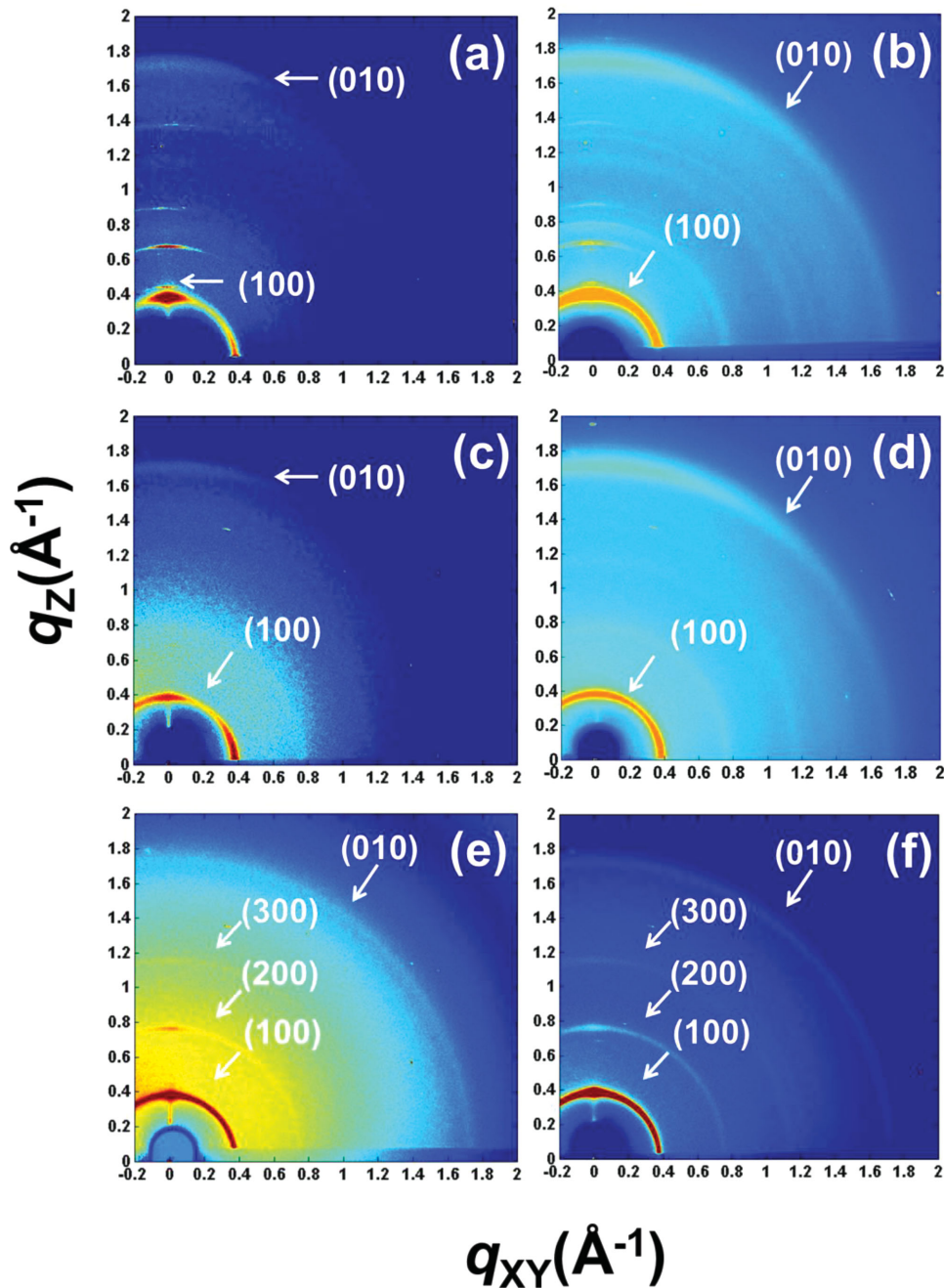**Figure 4.** Transmission-mode WAXS profiles of nonwoven PHTNF and PHTNF(II).

Figure 5. 2D GIXS patterns of aligned a,b) PHTNF, c,d) PHTNF(II), and e,f) PHTNF(II)-T with incident beam perpendicular (a,c,e) and parallel (b,d,f) to the fiber axis.

orientation in the electrical properties of polymeric nanofibers. Charge carriers can move effectively along highly extended and oriented chains even though the polymer is not crystallized.

In addition to P3HT, the electrospun nanofibers of poly(3-dodecylthiophene) (P3DDT) were produced in the same manner and were fabricated into OFETs. The electrical properties of P3DDT-beased devices without (PDDTNF) and with (PDDTNF(II)) the secondary electric field are displayed in Figure S2 (Supporting Information). The field-effect mobility of PDDTNF(II) is enhanced by a factor of 8.5 as shown in Table 1,

implying this method could be applied to other poly(3-alkylthiophene) fibers. The less improvement of mobility for P3DDT compared to P3HT may be due to the longer side chains that hinder the main-chain stretching under extensional forces.

3. Conclusions

We have shown that the introduction of a secondary electric field in the pathway of liquid jets during electrospinning

**ADVANCED
ELECTRONIC
MATERIALS**
www.advelectronicmat.de
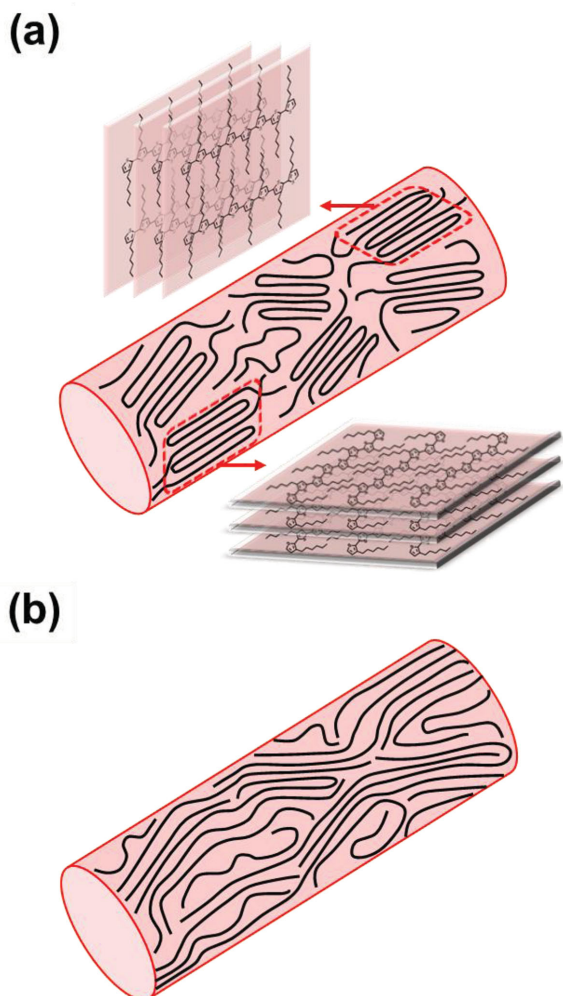
*Materials
Views*

www.MaterialsViews.com

Figure 6. Schematic of the microstructure of a) PHTNF and b) PHTNF(II). The black lines represent polymer backbones and the red frames in (a) define crystallites.

process can greatly enhance the electrical properties of P3HT and other poly(3-alkylthiophene) nanofibers. The charge carrier mobility of P3HT electrospun nanofibers is dramatically improved by more than 3 orders. This improvement is attributed to the strong extensional force provided by the secondary electric field that causes polymer chains to extend and align along the jet. The frozen stretched chains along the fibers then serve as a low-resistant route for charge carrier to transport. This work highlights the effective transport of charge carriers through one-dimensional intrachain delocalization along polymer chains and provides a simple way to fabricate high-performance OFETs.

4. Experimental Section

Materials: P3HT ($M_w \approx 50$ kg mol^{-1}, 90%–95% regioregular) and P3DDT ($M_w \approx 60$ kg mol^{-1}, 98.5% regioregular) were used as received from Reike Metals Inc. PMMA ($M_w \approx 350$ kg mol^{-1}) was purchased

from Sigma-Aldrich. Tetrabutylammonium perchlorate (TBAP, TCI) and Octadecyltrichlorosilane (ODTS, Sigma-Aldrich) were used as received without further purification. Chloroform (anhydrous 99.8%) and chlorobenzene (anhydrous 99.8%) were purchased from Sigma-Aldrich.

Electrospinning: A two-fluid coaxial electrospinning technique with a secondary electric field and modified collector was used to produce aligned core-shell nanofibers, as shown in Figure 1a.[21,43] Two syringes containing core and shell precursor solutions were used for producing the electrospun nanofibers. P3AT dissolved in anhydrous chloroform (50 mg mL^{-1}) overnight in a nitrogen-filled glovebox was used as the core solution. PMMA in anhydrous chlorobenzene (300 mg mL^{-1}) was used as the shell solution which contain 10 wt% of TBAP to increase conductivity and stabilize the cone-jet.[44] The core and shell solutions were fed into the coaxial capillaries by two syringe pumps (KD Scientific Model 100, USA). The feed rate of P3AT solution (core flow) was fixed at 0.1 mL h^{-1} while the feed rates of PMMA solution (shell flow) was operated at 1.0 mL h^{-1}. The tip of the core needle was connected to a high-voltage power supply (Chargemaster CH30P SIMCO, USA). The spinning voltage was set at 8.1–10 kV. To create the secondary electric field, a stainless steel ring of 8 cm diameter was placed 2 cm below the spinneret and connected to the power supply which provided the same voltage for the spinneret and the stainless steel ring. The collector made of electrically charged conductive aluminum disk (7 cm in diameter and 1.5 cm in height) with a rectangular hole (4 × 1 cm) was placed 13 cm below the tip of the needle (working distance) to collect the aligned nanofibers, similar to our previous reports.[21,45] To obtain uniform and aligned fibers, the cone-jet was kept stable during electrospinning process, which was monitored by a CCD camera (Xli 3M USB2.0 CCD camera, USA) and macro video zoom lens (OPTEM MVZL, USA). All experiments were carried out under ambient environment.

OFET Device Fabrication: Highly aligned coaxial electrospun nanofibers were transferred from the collector to silicon wafers with 200 nm SiO$_2$ layer as gate dielectrics. To reduce the hydrophilicity of wafer surface and immobilize the nanofibers during solvent extraction, the heavily n-type doped wafers were grafted with octadecyltrichlorosilane (ODTS) on the surface by the following procedure: the wafers were treated with ozone plasma for 5 min and then immersed into 10×10^{-3} M ODTS in anhydrous toluene for 2 h. Aligned core-shell electrospun nanofibers on wafers were immersed in acetone to remove shell PMMA. The top-contact source and drain gold electrodes with a thickness of 100 nm were deposited through a regular shadow mask. The channel length (L) and width (W) were 25 and 1500 μm, respectively.

Characterization: The images of field-emission scanning electron microscope FE-SEM were taken on JEOL JSM-6330F at an accelerating voltage of 10 kV. DSC measurements were performed under nitrogen atmosphere at a heating rate of 5 °C min^{-1} by TA Instruments DSC-Q100. Indium was employed for the temperature calibration. The molecular packing in P3HT electrospun nanofibers was investigated by transmission-mode X-ray diffraction (XRD) and two-dimensional grazing incidence X-ray scattering (2-D GIXS) on beamline 17A1 of National Synchrotron Radiation Research Center, Taiwan. Output and transfer characteristics of nanofiber-based OFET devices were measured using Keithley 4200 semiconductor parametric analyzer. The electrical measurements were conducted in a nitrogen-filled glovebox. Threshold voltages (V_{TH}) of the devices were determined from a linear relationship between the square root of drain current $I_{DS}^{1/2}$ versus gate voltage V_{GS} by extrapolating the measured data to $I_{DS} = 0$ A. In the saturation region, the modified equation for the current, $I_{DS} = \mu(CL^{-2})(V_{GS} - V_{TH})^2$, was used to obtain the charge carrier mobility (μ). The modification is due to the unconventional semiconducting cylinder over a planar dielectric layer. The capacitance per unit length (CL^{-1}) with respect to the back gate is described by $2\pi\varepsilon\varepsilon_0(\ln(2hr^{-1}))^{-1}$, where r is the radius of the fiber, h is the dielectric layer thickness (200 nm), and ε is the average dielectric constant (≈2.5) of dielectric layer.
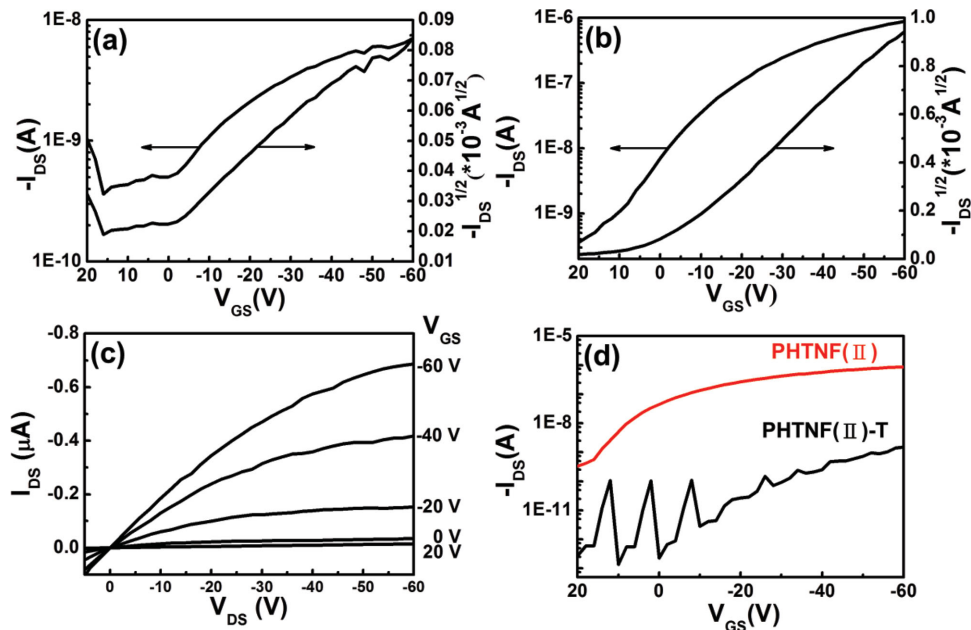
Figure 7. The transfer characteristics of a) PHTNF and b) PHTNF(II), c) the output characteristic of PHTNF(II), and d) the transfer characteristics of PHTNF(II) before and after thermal treatment.

Table 1. Fiber diameters and electrical properties of electrospun nanofibers-based OFET devices.

Sample	Diameter [nm]	μ_{ave} [cm^2 V^{-1} s^{-1}][a]	$I_{on/off}$	V_{TH} [V]
PHTNF	414 ± 52	$(1.54 \pm 0.58) \times 10^{-4}$	1.96×10^{1}	20
PHTNF(II)	144 ± 30	$(1.62 \pm 0.29) \times 10^{-1}$	2.47×10^{3}	1.5
PHTNF(II)-T	708 ± 72	$(2.26 \pm 0.73) \times 10^{-5}$	1.09×10^{4}	22
PDDTNF	482 ± 62	$(3.58 \pm 0.37) \times 10^{-3}$	1.26×10^{5}	0.8
PDDTNF(II)	261 ± 65	$(3.06 \pm 0.14) \times 10^{-2}$	9.89×10^{4}	2

[a]The average charge carrier mobility obtained from measuring at least three OFET devices.

Supporting Information

Supporting Information is available from the Wiley Online Library or from the author.

[1] H. Klauk, *Organic Electronics: Materials, Manufacturing, and Applications*, Wiley-VCH, Weinheim **2006**.

[2] Z. Bao, J. Locklin, *Organic Field-Effect Transistors*, CRC Press, New York **2007**.

[3] H. Sirringhaus, P. J. Brown, R. H. Friend, M. M. Nielsen, K. Bechgaard, B. M. W. Langeveld-Voss, A. J. H. Spiering, R. A. J. Janssen, E. W. Meijer, P. Herwig, D. M. de Leeuw, *Nature* **1999**, *401*, 685.

[4] S. Cho, K. Lee, J. Yuen, G. M. Wang, D. Moses, A. J. Heeger, M. Surin, R. Lazzaroni, *J. Appl. Phys.* **2006**, *100*, 114503.

[5] H. Sirringhaus, P. J. Brown, R. H. Friend, M. M. Nielsen, K. Bechgaard, B. M. W. Langeveld-Voss, A. J. H. Spiering, R. A. J. Janssen, E. W. Meijer, *Synth. Methods* **2000**, *111*, 129.

[6] R. A. Street, J. E. Northrup, A. Salleo, *Phys. Rev. B* **2005**, *71*, 165202.

[7] Y. D. Park, H. S. Lee, Y. J. Choi, D. Kwak, J. H. Cho, S. Lee, K. Cho, *Adv. Funct. Mater.* **2009**, *19*, 1200.

[8] H. Yang, T. J. Shin, L. Yang, K. Cho, C. Y. Ryu, Z. Bao, *Adv. Funct. Mater.* **2005**, *15*, 671.

[9] R. Zhang, B. Li, M. C. Iovu, M. Jeffries-El, G. Sauvé, J. Cooper, S. Jia, S. Tristram-Nagle, D. M. Smilgies, D. N. Lambeth, R. D. McCullough, T. Kowalewski, *J. Am. Chem. Soc.* **2006**, *128*, 3480.

[10] B. W. Boudouris, V. Ho, L. H. Jimison, M. F. Toney, A. Salleo, R. A. Segalman, *Macromolecules* **2011**, *44*, 6653.

[11] M. Chang, D. Choi, B. Fu, E. Reichmanis, *ACS Nano* **2013**, *7*, 5402.

[12] D. M. DeLongchamp, R. J. Kline, Y. Jung, D. S. Germack, E. K. Lin, A. J. Moad, L. J. Richter, M. F. Toney, M. Heeney, I. McCulloch, *ACS Nano* **2009**, *3*, 780.

[13] S. Nagamatsu, W. Takashima, K. Kaneto, Y. Yoshida, N. Tanigaki, K. Yase, *Appl. Phys. Lett.* **2004**, *84*, 4608.

[14] D. Gargi, R. J. Kline, D. M. DeLongchamp, D. A. Fischer, M. F. Toney, B. T. O'Connor, *J. Phys. Chem. C* **2013**, *117*, 17421.

[15] B. O'Connor, R. J. Kline, B. R. Conrad, L. J. Richter, D. Gundlach, M. F. Toney, D. M. DeLongchamp, *Adv. Funct. Mater.* **2011**, *21*, 3697.

[16] S. Nagamatsu, W. Takashima, K. Kaneto, Y. Yoshida, N. Tanigaki, K. Yase, K. Omote, *Macromolecules* **2003**, *36*, 5252.

[17] Y. K. Lan, C. I. Huang, *J. Phys. Chem. B* **2009**, *113*, 14555.

[18] G. Derue, S. Coppée, S. Gabriele, M. Surin, V. Geskin, F. Monteverde, P. Leclère, R. Lazzaroni, P. Damman, *J. Am. Chem. Soc.* **2005**, *127*, 8018.

[19] W.-Y. Lee, J. H. Oh, S. L. Suraru, W.-C. Chen, F. Würthner, Z. Bao, *Adv. Funct. Mater.* **2011**, *21*, 4173.

[20] A. Babel, D. Li, Y. N. Xia, S. A. Jenekhe, *Macromolecules* **2005**, *38*, 4705.

[21] J.-Y. Chen, C.-C. Kuo, C.-S. Lai, W.-C. Chen, H.-L. Chen, *Macromolecules* **2011**, *44*, 2883.

[22] J.-Y. Chen, H.-C. Wu, Y.-C. Chiu, W.-C. Chen, *Adv. Energy Mater.* **2014**, *4*, 1301665.

[23] D. Li, A. Babel, S. A. Jenekhe, Y. Xia, *Adv. Mater.* **2004**, *16*, 2062.

[24] C.-J. Lin, J.-C. Hsu, J.-H. Tsai, C.-C. Kuo, W.-Y. Lee, W.-C. Chen, *Macromol. Chem. Phys.* **2011**, *212*, 2394.

[25] S. K. Hwang, S.-Y. Min, I. Bae, S. M. Cho, K. L. Kim, T.-W. Lee, C. Park, *Small* **2014**, *10*, 1976.

[26] S.-Y. Min, T.-S. Kim, B. J. Kim, H. Cho, Y.-Y. Noh, H. Yang, J. H. Cho, T.-W. Lee, *Nat. Commun.* **2013**, *4*, 1773.

[27] J. M. Deitzel, J. D. Kleinmeyer, J. K. Hirvonen, N. C. Beck Tan, *Polymer* **2001**, *42*, 8163.

[28] O. Karatay, M. Dogan, Micro*Nano Lett.* **2011**, *6*, 858.

[29] G. Taylor, *Proc. R. Soc. A* **1969**, *313*, 453.

[30] J. Doshi, D. H. Reneker, *J. Electrostatics* **1995**, *35*, 151.

[31] M. V. Kakade, S. Givens, K. Gardner, K. H. Lee, D. B. Chase, J. F. Rabolt, *J. Am. Chem. Soc.* **2007**, *129*, 2777.

[32] T. Kongkhlang, K. Tashiro, M. Kotaki, S. Chirachanchai, *J. Am. Chem. Soc.* **2008**, *130*, 15460.

[33] A. Camposeo, I. Greenfeld, F. Tantussi, S. Pagliara, M. Moffa, F. Fuso, M. Allegrini, E. Zussman, D. Pisignano, *Nano Lett.* **2013**, *13*, 5056.

[34] X. Cui, L. Li, F. Xu, *Appl. Phys. A* **2011**, *103*, 167.

[35] R. Inai, M. Kotaki, S. Ramakrishna, *Nanotechnology* **2005**, *16*, 208.

[36] C. R. Snyder, R. C. Nieuwendaal, D. M. DeLongchamp, C. K. Luscombe, P. Sista, S. D. Boyd, *Macromolecules* **2014**, *47*, 3942.

[37] L. H. Sperling, *Introduction to Physical Polymer Science*, Wiley, Hoboken, NJ **2006**.

[38] S. Malik, A. K. Nandi, *J. Polym. Sci., Part B: Polym. Phys.* **2002**, *40*, 2073.

[39] F. P. V. Koch, M. Heeney, P. Smith, *J. Am. Chem. Soc.* **2013**, *135*, 13699.

[40] J. Byun, Y. Kim, G. Jeon, J. K. Kim, *Macromolecules* **2011**, *44*, 8558.

[41] D. Chen, W. Zhao, T. P. Russell, *ACS Nano* **2012**, *6*, 1479.

[42] D. E. Johnston, K. G. Yager, H. Hlaing, X. Lu, B. M. Ocko, C. T. Black, *ACS Nano* **2013**, *8*, 243.

[43] H. J. Yu, S. V. Fridrikh, G. C. Rutledge, *Adv. Mater.* **2004**, *16*, 1562.

[44] A. G. MacDiarmid, W. E. Jones, I. D. Norris, J. Gao, A. T. Johnson, N. J. Pinto, J. Hone, B. Han, F. K. Ko, H. Okuzaki, M. Llaguno, *Synth. Methods* **2001**, *119*, 27.

[45] C.-C. Kuo, C.-T. Wang, W.-C. Chen, *Macromol. Mater. Eng.* **2008**, *293*, 999.